NJC

ROYAL SOCIETY OF CHEMISTRY

PAPER

View Article Online
View Journal | View Issue

Cite this: *New J. Chem.*, 2023, **47**, 6932

An effective strategy for CO_2 reduction to C1 products using Cu-embedded MoS_2 electrocatalyst: DFT study†

Thamarainathan Doulassiramane,[a] Natarajan Arumugam,[b] Abdulrahman I. Almansour,[b] Sakkarapalayam M. Mahalingam[c] and Ramanathan Padmanaban *[a]

Excessive emission of CO_2 has caused a critical greenhouse effect that is emerging as a major threat to the environment. Electrocatalytic reduction of CO_2 is an advanced technology where chemically inert CO_2 is reduced and can be used to produce value-added fuels or chemicals. In this work, the electrocatalytic performance of a single Cu atom embedded in a MoS_2 monolayer with a sulfur vacancy for the electroreduction of CO_2 is studied using density functional theory (DFT) with dispersion correction. The single Cu atom is stably located in the sulfur vacancy of the MoS_2 monolayer. The multiple pathways explored here involve proton–electron pair transfer in the CO_2 reduction reaction (CO_2RR) to yield a variety of C1 products, such as HCOOH, CO, CH_3OH and CH_4. These pathways were examined using the corresponding free energy profiles and overpotentials. Among the different C1 products, CH_4 formation is more favored *via* the following optimized pathway: $*CO_2 \rightarrow *OCHO \rightarrow *OCHOH \rightarrow *OCH_2OH \rightarrow *OCH_2 \rightarrow *OCH_3 \rightarrow *OHCH_3 \rightarrow *OH + CH_4 \rightarrow H_2O$. The MoS_2 monolayer with embedded Cu has enhanced CO_2RR activity with an appreciably low overpotential compared to pristine MoS_2. This study provides a deep understanding of the structure–reaction relationships and various mechanistic pathways of the CO_2RR, and could aid in the design of high-performance single-atom electrocatalysts.

Received 15th February 2023,
Accepted 1st March 2023

DOI: 10.1039/d3nj00716b

rsc.li/njc

1 Introduction

Over the years, the increasing world population and the advancement of society have increased the stress caused by global energy consumption, which is largely met by burning fossil fuels leading to excessive emission of carbon dioxide (CO_2) into the global atmosphere.[1] This steady increase in CO_2 concentration is causing serious environmental issues, such as global warming, climate change and an imbalance in Earth's carbon cycle.[2] To mitigate these issues, various strategies have been used in the recent past. The traditional methods include underground storage,[3] physical and chemical separation,[4,5] photosynthesis,[6] and biological conversion,[7] but their technologies are expensive and they have safety issues.[8] So, an alternative and effective method is required, and the electrocatalytic CO_2 reduction reaction (CO_2RR) allows direct conversion of CO_2 into high-value added fuels or commodity chemicals, *e.g.*, alcohols or hydrocarbons, powered by excess electricity from renewable energy sources (solar, wind and hydro-power).[9] This is a promising way to solve energy-related issues and finding highly effective catalysts which can carry out this conversion has become a hot topic.

In the recent past, several authors have extensively studied the electrochemical CO_2RR on various metal electrodes, such as Au, Ag and Cu, which activate the inert CO_2 and convert it into HCOOH, CO, CH_3OH and CH_4.[10–12] Despite the great progress made, the CO_2RR suffers from sluggish kinetics, high overpotential, low faradaic efficiency, poor selectivity and strong competition with the hydrogen evolution reaction (HER).[13,14] So, it is a challenging task to find an effective low-cost electrocatalyst with low overpotential and high product selectivity. To tackle these problems, many materials were designed and explored for the synthesis of novel electrode materials including single-atom catalysts (SACs).[15] SACs possess unique properties such as high selectivity, activity and atom-utilization efficiency, uniform active sites and their ability to bridge the

[a] *Department of Chemistry, School of Physical Chemical and Applied Sciences, Pondicherry University, Puducherry-605 014, India. E-mail: rpn.che@pondiuni.edu.in*
[b] *Department of Chemistry, College of Science, King Saud University, P.O. Box 2455, Riyadh 11451, Saudi Arabia*
[c] *Department of Chemistry, Purdue University, 720 Clinic Drive, West Lafayette, Indiana 47907, USA*

† Electronic supplementary information (ESI) available. See DOI: https://doi.org/10.1039/d3nj00716b

gap between homogeneous and heterogeneous catalysts.[16,17] Huge interest in SACs has been established since the successful fabrication of an iron-oxide supported Pt SAC by Zhang *et al.* in 2011.[18] From both experimental and theoretical studies, various SACs supported on two-dimensional (2D) materials have been reported to be active for electrocatalytic conversions, including the CO_2RR, with better efficiency and durability.[19–22]

To further improve the efficiency of SACs, appropriate selection of the supporting material is needed. Apart from metal and metal-oxide supported SACs, molybdenum disulfide (MoS_2) layered materials known as transition metal dichalcogenides (TMDCs) have been receiving a lot of research attention due to their direct band gap in the monolayer regime and for being low-cost semiconductor materials. MoS_2 has a 2D layered structure similar to graphene, with the individual layers stacked upon each other through weak van der Waals (vdW) forces to form the bulk. Further, MoS_2 has attracted much attention in the development of sensors,[23] hydrogen storage,[24] battery electrodes,[25] transistors,[26] nanoelectronics and optoelectronics,[27] due to its high surface area, thermal stability and high electrical conductivity.[28,29] For the purpose of CO_2 activation, only the edges of MoS_2 are active, whereas the basal plane is inert.[30,31] However, the basal plane has a higher surface area to volume ratio than the edges. So, it is desirable to activate the basal plane,[32] which will improve the catalytic activity for the CO_2RR. Theoretical studies have shown that the adsorption ability of gas molecules on MoS_2 increases when depositing transition and noble metals (Ti, Ni, Co, Pd, Au, Fe, *etc.*,) on the basal plane.[33–36] Single metal atoms supported on the MoS_2 layer provide excellent performance towards various reactions.[37–39] Additionally, earlier experimental and theoretical studies showed that various structural defects can be created in the monolayer.[40,41] One such defect is the sulfur vacancy, which can be introduced in MoS_2 in a controlled way by electron irradiation. Interestingly, Liu *et al.* have synthesized MoS_2 with a Co atom embedded in a sulfur vacancy in the basal plane and reported excellent activity for the conversion of 4-methylphenol to toluene with high thermal stability.[42]

From earlier studies, it is well known that Cu as an electrocatalyst has good CO_2 reducing ability.[12,43,44] In 2020, Joseph *et al.* experimentally synthesized Cu-doped MoS_2 and reported a significant enhancement in electrical conductivity compared to the pristine MoS_2 (with a stable 1H phase structure).[45] In spite of several reports, mechanical insights into the formation of different C1 products with a lower overpotential are still unavailable and challenging to obtain, and this has driven us to carry out the present study. Here, we provide a novel approach for the efficient reduction of CO_2 through a coupled proton–electron transfer. We investigate the catalytic activity on a single Cu atom embedded in a MoS_2 monolayer and optimize the electrocatalytic behavior in the basal plane of the TMDC material.

For the purpose of the CO_2RR on Cu–MoS_2, we employed periodic density functional theory (DFT), a well-known tool, to explain the mechanism of various electrocatalytic reactions. The stability of the Cu–MoS_2 surface model, adsorption energy of intermediates, Bader charges, density of states (DOS), and reaction free energies of each elementary step have been calculated. The selectivity for CO_2RR *vs.* HER on Cu–MoS_2 and pristine MoS_2 was also investigated. The reduction of CO_2 on the TMDC material with embedded Cu can produce more than 14 products with different selectivities. The overpotential (η) and limiting potential (U_L) calculated from potential-determining steps (PDSs) for each reduction pathway, *e.g.*, from CO_2 to HCOOH, CO, CH_3OH, and CH_4, were analyzed to elucidate the catalytic activity. Thus, this study attempted to predict the promise of the Cu–MoS_2 SAC as an electrocatalyst for selective CO_2 reduction to produce different value-added chemicals.

2 Computational details

All the spin-polarized electronic structure calculations were carried out within the DFT framework[46] implemented in the Vienna *ab initio* Simulation Package (VASP).[47] The core electrons were treated using the projector augmented-wave (PAW) pseudopotential[48] and a plane-wave basis set[49] with a kinetic energy cutoff of 450 eV was used. The electron exchange–correlation effects were described by the Perdew–Burke–Ernzerhof (PBE) functional of the generalized gradient approximation (GGA).[50] To include the vdW interaction, Grimme's empirical dispersion-corrected D3-functional was used.[51] The Brillouin zone was sampled using Monkhorst–Pack[52] *k*-point meshes of $3 \times 3 \times 1$ and $6 \times 6 \times 1$ for the different geometry optimization and electronic structure calculations. The convergence criterion for geometry optimization with self-consistent field iteration was set as 10^{-6} eV, and the forces acting on atoms were set to 0.02 eV $Å^{-1}$.

The MoS_2 monolayer was modeled by cleaving the bulk MoS_2 structure in the (001) direction. Subsequently, a 4×4 supercell containing 16 Mo and 32 S atoms was generated with a vacuum space of 15 Å in the *z*-direction to avoid unfavorable interactions between its periodic images. A sulfur defect was introduced, *i.e.*, one sulfur atom was replaced with a Cu atom, to obtain the MoS_2 monolayer with embedded Cu. All the atoms in the supercell were allowed to relax during the optimization. By employing Bader charge analysis[53,54] and charge density difference (CDD), the charge transfer and redistribution were investigated for the adsorbate–surface system.

Next, the binding energy (E_b) of Cu in MoS_2 with a sulfur vacancy was calculated from the difference between the total energy of MoS_2 with embedded Cu (E_{Cu-MoS_2}) and the sum of the energies of the isolated Cu atom ($E_{Cu\text{-}atom}$) and MoS_2 with a sulfur vacancy ($E_{Svc\text{-}MoS_2}$):

$$E_b = E_{Cu-MoS_2} - (E_{Cu\text{-}atom} + E_{Svc\text{-}MoS_2}). \quad (1)$$

The adsorption energies (E_{ads}) of the CO_2 and various intermediates of the CO_2RR ($E_{adsorbate}$) are described by the equation,

$$E_{ads} = E_{adsorbate/Cu-MoS_2} - E_{adsorbate} - E_{Cu-MoS_2}, \quad (2)$$

where $E_{adsorbate/Cu-MoS_2}$, $E_{adsorbate}$, and E_{Cu-MoS_2} are the total energy of the adsorbate at the surface, the energy of the adsorbate alone and the energy of the surface, respectively.

The Gibbs free energy change (ΔG) of each elementary step was calculated by employing the Computational Hydrogen Electrode (CHE) model developed by Nørskov *et al.*,[55] and is given by the following equation:

$$\Delta G = \Delta E + \Delta E_{ZPE} - T\Delta S + \Delta G_U + \Delta G_{pH}, \quad (3)$$

where ΔE is the change in reaction energy obtained from the DFT method; ΔE_{ZPE} and ΔS are the zero-point energy (ZPE) and entropy change for each step, determined from the frequency calculations of the adsorbed intermediates; and T is the temperature (298.15 K). $\Delta G_U = -neU$, where n is the number of transferred proton–electron pairs (PEPs) and U is the applied electrode potential; $\Delta G_{pH} = -k_B T \ln 10 \times pH$ is the free energy contribution to the change in H^+ ion concentration, where pH is set to 0 in order to maintain strongly acidic conditions. The limiting potential (U_L) is the most positive free energy change (ΔG_{max}) among all the electrochemical steps in the chosen pathway, and it is given by a simple relation:

$$U_L = -\Delta G_{max}/e. \quad (4)$$

Finally, the overpotential (η), defined as the electrocatalytic activity descriptor of Cu–MoS_2 for each pathway, was obtained by subtracting the limiting potential from its equilibrium potential (U_{eq}), given as:

$$\eta = U_{eq} - U_L. \quad (5)$$

3 Results and discussion

3.1 Structure and stability of CO_2 on Cu–MoS_2

Before we study the CO_2RR activity of the Cu–MoS_2 system, it is very important to investigate the stability of the single Cu atom in the MoS_2 monolayer with a sulfur vacancy. The DFT optimized structure of the SAC model is shown in Fig. 1(a), with an average bond length of ~2.60 Å between the Cu and its three neighboring Mo atoms. As the Mo–Cu bond lengths are usually longer than the Mo–S bond, this makes the Cu protrude from the S-plane. The calculated binding energy (E_b) of the doped Cu atom in the MoS_2 monolayer with a sulfur vacancy is about −3.38 eV, which means that Cu is held strongly in the sulfur vacancy. To validate this, we analyzed the diffusion of Cu to nearby sites on the MoS_2 surface, *i.e.*, on top of the nearest Mo atom and in a hollow site, as shown in Fig. S1 (see ESI†). By performing nudged elastic band (NEB) calculations, the energy barriers/transition states (TSs) for the top and hollow sites are found to be 1.67 and 1.59 eV, respectively. Because of these relatively large energy barriers, the Cu atom is firmly held in the sulfur vacancy of the MoS_2 monolayer. In order to confirm the presence of doped-Cu species, the total density of states (TDOS) is calculated for the Cu–MoS_2 SAC model and compared with the pristine MoS_2 monolayer, as shown in Fig. 1(b). There is a noticeable peak with non-zero TDOS appearing at the Fermi energy level for the Cu-doped MoS_2, whereas such a peak is not seen for the pristine MoS_2. Further, there are two peaks near the Fermi level in the projected density of states (PDOS) of Cu–MoS_2 (see Fig. S2 in ESI†), showing the localized features around the 3d orbital of the Cu atom. This is called a metal-induced gap state, composed of Cu-3d and Mo-4d orbitals. From the isosurface of the charge density difference (shown as an inset in Fig. 1(b)), we can see charge redistribution localized around the Cu–Mo bond, which confirms the electron overlap between the embedded Cu and nearby Mo atoms. This result agrees well with other theoretical findings.[56] So, we confirm that the Cu embedded in MoS_2 is stable, as is the case with other doped metals, such as Ni, Mn, Fe and Co, in MoS_2.[38,57,58]

The initial activation step, CO_2 adsorption on the catalyst ($CO_2 \rightarrow *CO_2$), is a very important step that determines the activity of the CO_2RR. The change in the fundamental geometrical parameters of CO_2 reveals the CO_2RR activity of the SAC. In order to gain insights into the CO_2 adsorption on Cu–MoS_2, the adsorption energy, density of states (DOS), charge density difference and Bader charges are calculated. The optimized structure of CO_2 adsorbed on the Cu–MoS_2 surface is shown in Fig. 2, along with its isosurface structure. As mentioned, the Cu atom on the basal plane of the Cu–MoS_2 surface is the active center for the CO_2RR. It can be seen from Fig. 2 that the CO_2 is adsorbed vertically on the Cu atom *via* an O atom rather than carbon, with an adsorption distance (d_{O-Cu}) of ~2.139 Å and adsorption energy E_{ads} of −0.474 eV. The negative E_{ads} shows

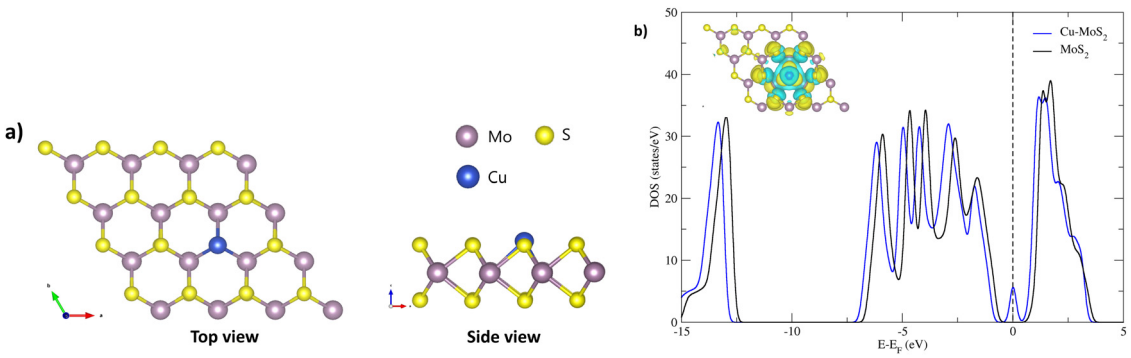

Fig. 1 (a) Optimized structural geometry of the MoS_2 monolayer with embedded Cu with E_b = −3.38 eV, obtained using the DFT-D3 method. (b) Total density of states of Cu–MoS_2 with the isosurface of the charge density difference.

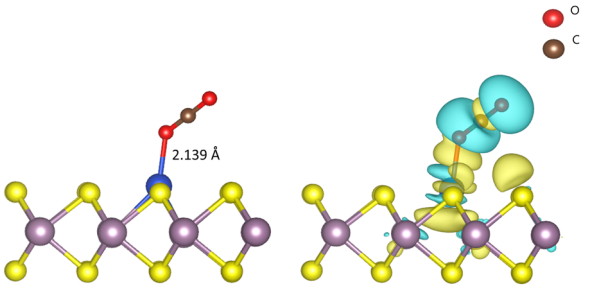

Fig. 2 Representation of the optimized structure (left-hand side) of CO_2 adsorbed on Cu–MoS_2 along with the isosurface of the charge density difference (right-hand side). The isosurface value is kept as 0.002 e bohr^{-3}. The yellow and cyan regions show charge accumulation and depletion, respectively.

that the CO_2 adsorption process is favorable in view of thermodynamic stability. According to Bader charge analysis, there is a small partial negative charge that is transferred from Cu to the antibonding (2π) orbital of CO_2, which extends one C–O_1 bond length to $\sim$1.186 Å, from the 1.17 Å of free CO_2. From the isosurface of the charge density difference (see Fig. 2, right-hand side), it is found that charge redistribution mainly occurs between CO_2 and the embedded Cu atom. Similarly, the PDOS plot shown in Fig. S2 (ESI†) also shows distinct hybridization peaks between the Cu-3d orbital and the O-2p orbital of CO_2, mainly in the range of -5.0 eV. This confirms the strong interaction between the dopant (Cu) and CO_2 molecule. So, the bond formation occurs through the overlap of electron density from Cu-3d and O-2p, and thereby CO_2 is likely to be chemisorbed on the Cu–MoS_2 monolayer.

3.2 Electrochemical reduction of CO_2 on the Cu–MoS_2 SAC

In the present Cu–MoS_2 SAC model, the CO_2 reduction process is carried out by a proton–electron pair (PEP: $H^+ + e^-$) transfer in each reaction step. The schematic representation of all possible pathways for the electrocatalytic reduction of CO_2 to C1 products is shown in Scheme 1, combining the conclusions from previous reports.[59,60] DFT-D3 calculations were performed to obtain the optimized structures and free energies of all possible intermediates and products, and to determine the preferable pathway for CO_2RR. The first hydrogenation (PEP transfer) of *CO_2 leads to the two different intermediates, *i.e.*, *COOH and *OCHO, where * denotes surface-adsorbed species. The lowest energy pathway, *i.e.*, that with the lowest positive free energy change between any two steps, is determined for the C1 products, namely HCOOH, CO, CH_3OH and CH_4. It is worth pointing out that the direct attack of *H on the Cu atom is also possible, but the free energy of interactions between them is very small, as will be discussed in the following subsection.

3.2.1 Two electron pathway: CO_2 to CO or HCOOH. The CO_2RR involving $2e^-$ transfer yields the products CO and HCOOH. The free energy diagrams of CO_2 reduction to CO and HCOOH are shown in Fig. 3.

As mentioned above, the first step of the CO_2RR is CO_2 hydrogenation *via* PEP transfer with two possible intermediates:

(i) H^+ attacks the O atom: * + CO_2 + H^+ + e^- → *COOH (carboxyl), ΔG = 0.68 eV, and

(ii) H^+ attacks the C atom: * + CO_2 + H^+ + e^- → *OCHO (formate), ΔG = 0.24 eV,

The next hydrogenation step leads to the formation of CO (with dehydration) and HCOOH products, respectively. In the case of pristine MoS_2, this hydrogenation process is unfavorable due to a high ΔG (2.24 and 1.87 eV for *OCHO and *COOH intermediates), and therefore we employed the doping strategy here to reduce the limiting potential (U_L). It is known that the catalytic activity of electrocatalysts can be effectively characterized by evaluating the limiting potential. The free energy change for the said intermediates formed on Cu–MoS_2 is significantly reduced, and the corresponding U_L values are -0.68 V (3 times lower than that of the pristine monolayer) and -0.24 V (10 times lower than that of the pristine monolayer), respectively. Further, the *CO_2 is preferentially hydrogenated to *OCHO on the Cu–MoS_2 electrocatalyst by forming a Cu–O bond. This trend is explained by analyzing the PDOS of the intermediates *OCHO and *COOH, as shown in Fig. 4. This clearly shows that the overlap between Cu-3d and O-2p of OCHO is higher than that with C-2p of COOH. In order to verify the selectivity of the CO_2RR over the HER, the free energy change and adsorption energies for the direct (first) hydrogenation on the Cu-doped and pristine MoS_2 monolayers are also calculated, and the results are presented in Fig. S3 (ESI†). The calculated adsorption energies (including dispersion correction), bond distances of adsorbed species from the active site (Cu atom) and the Bader charges of all possible intermediates are given in Table 1. It can be seen from Fig. 3, Fig. S3 (ESI†) and Table 1 that *OCHO (CO_2RR) is more easily formed on Cu–MoS_2 than *COOH (CO_2RR) and *H (HER), due to the stronger electron interaction in the first hydrogenation step. Further, the free energy change for the HER on Cu–MoS_2 is 0.58 eV and that for CO_2RR is only 0.24 eV. To clarify this, the E_{ads} values of *OCHO, *COOH and H* on Cu–MoS_2 are found to be -2.749, -1.938 and 0.419 eV, respectively (see Table 1). This indicates that *OCHO and *COOH strongly adsorb on the surface and undergo hydrogenation effectively, whereas the HER process is inhibited as the adsorption between *H and the Cu active center is weaker. Furthermore, when the active centre of the catalyst is occupied by the *OCHO/*COOH species, the formation of *H is difficult, which causes the suppression of the HER in the present study.

With the above findings, we proceed with the next hydrogenation step, which leads to the simple C1 products *CO and *HCOOH (see Scheme 1). In the two-electron pathway, the second hydrogenation steps are *OCHO + H^+ + e^- → *OCHOH → * + HCOOH, and *COOH + H^+ + e^- → *CO + H_2O → * + CO, respectively. Note that simple protonation is involved in the former path, whereas the protonation is followed by dehydration in the latter path. It is further noticed that both reactions, forming formic acid (*HCOOH) and carbon monoxide (*CO) on the Cu–MoS_2 monolayer, are slightly exothermic (~ -0.11 eV). Cu–MoS_2 is more active towards CO_2 reduction to HCOOH with a limiting potential of -0.24 V, which is better than those of the

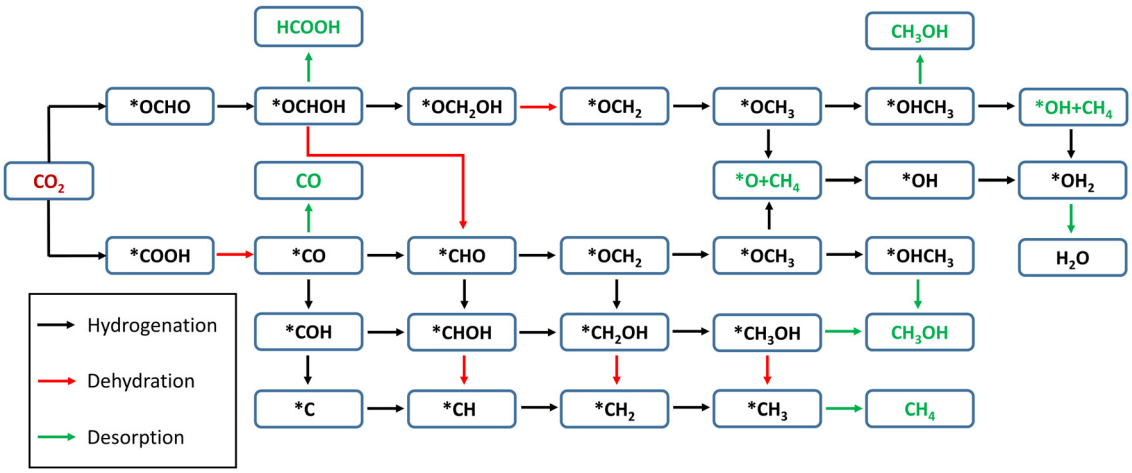

Scheme 1 Schematic representation of multiple pathways of electrochemical reduction of CO_2 to C1 products on the MoS_2 monolayer with embedded Cu. Red and green arrows are used to distinguish the significant steps, namely dehydration and desorption, respectively.

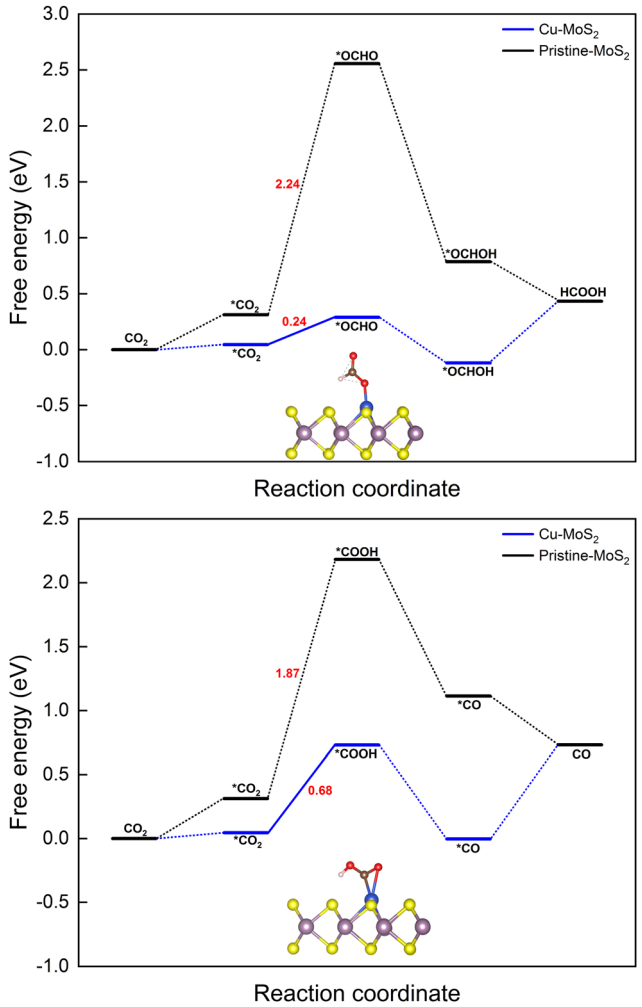

Fig. 3 Gibbs free energy diagrams for the CO_2RR towards the products HCOOH (top) and CO (bottom) on the MoS_2 monolayer with embedded Cu at 0 V *vs.* the RHE.

pristine MoS_2 and other reported SACs for CO_2 reduction to HCOOH.[61–63] From the ΔG of desorption for the two-electron C1 products using the SAC, it is seen that HCOOH (0.55 eV) can be more easily desorbed than CO (0.75 eV). However, theoretical studies have demonstrated that the relative adsorption energies of *OCHOH and *CO determine whether HCOOH and CO are the main products or reaction intermediates. Conversely, the adsorption energies of *OCHOH (−1.03 eV) and *CO (−1.27 eV) show that they are possible reaction intermediates for further hydrogenation.

3.2.2 Six electron pathway: CH_3OH formation. Unlike the two-electron pathway, the CO_2 reduction process involving $6e^-$ transfer opens up multiple channels in order to form the product methanol (CH_3OH). We here propose six different pathways for the electrocatalytic reduction of CO_2 to CH_3OH. The free energies of all possible intermediates formed on pristine MoS_2 and Cu–MoS_2 surfaces are calculated, and shown in Fig. 5.

It is found that *CO is a key intermediate formed *via* protonation followed by dehydration for proposed paths 1 to 4, whereas *OCHOH is formed *via* only protonation for paths 5 and 6. Thus, the corresponding hydrogenation reaction step is the potential-determining step (PDS), *i.e.*, while the *CO hydrogenation to *CHO(*COH) is the PDS for path 1–3(4), conversion of *OCHOH to *CHO and *OCHOH to *OCH_2OH is the PDS for the paths 5 and 6, respectively, for the Cu–MoS_2 SAC. In the case of pristine MoS_2, the first hydrogenation step itself (*CO_2 to *COOH) becomes the PDS with a large free energy change of 2.24 eV. The catalyst performance is determined by calculating the overpotential (η). As the negative limiting potential increases, the overpotential decreases, *i.e.*, the energy that needs to be supplied externally *via* an applied potential (U) is reduced. The calculated limiting potential and overpotential for the PDS of each path for the CO_2RR to CH_3OH on Cu–MoS_2 are given in Table 2.

An overpotential of only 0.86 V is required for this electrochemical conversion on Cu–MoS_2 *via* path 6, compared to the

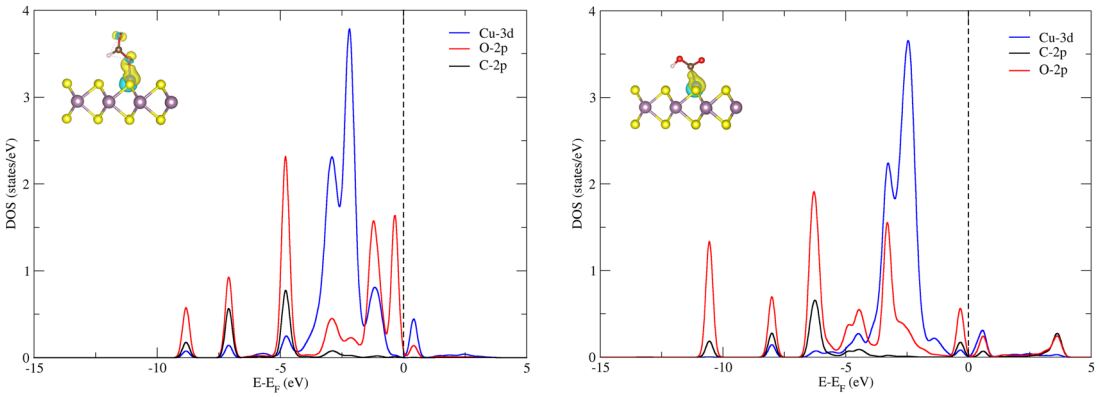

Fig. 4 Projected density of states (PDOS) plots for O-2p and C-2p of *OCHO (left) and *COOH (right), along with Cu-3d of Cu–MoS_2 and their isosurfaces of charge density difference. The isosurface value is kept as 0.002 e bohr^{-3}.

Table 1 Intermediates with their adsorption energies (E_{ads}), bond distances from the Cu active site to the C or O atom (d_{Cu-C} and d_{Cu-O}) and Bader charges (Q) of Cu, C, and O

Intermediates	E_{ads} (eV)	d_{Cu-C} (Å)	d_{Cu-O} (Å)	Q_{Cu} (e)	Q_C (e)	Q_O (e)
*CO_2	−0.474	—	2.13	0.20	2.12	−1.10
*H	0.419	—	—	0.13	—	—
*COOH	−1.938	1.91	—	0.21	1.30	−1.04
*OCHO	−2.749	—	1.83	0.30	1.53	−1.11
*OCHOH	−1.028	—	1.99	0.23	1.46	−1.14
*CO	−1.274	1.86	—	0.21	0.97	−1.03
*OCH_2OH	−2.470	—	1.73	0.30	0.97	−1.05
*CHO	−1.515	1.96	—	0.15	0.72	−0.99
*COH	−1.932	1.79	—	0.17	0.52	−1.14
*OCH_2	−0.858	—	1.94	0.24	0.74	−1.06
*CHOH	−2.418	1.88	—	0.16	0.40	−1.07
*C	−2.503	1.79	—	0.16	−0.27	—
*OCH_3	−2.765	—	1.78	0.31	0.45	−1.02
*CH	−3.135	1.79	—	0.22	−0.38	—
*CH_2OH	−1.643	1.94	—	0.18	0.23	−1.08
*CH_2	−2.530	1.85	—	0.20	−0.35	—
*$OHCH_3$	−1.135	—	2.02	0.22	0.33	−1.13
*O + CH_4	−0.417	—	1.75	0.33	—	−0.62
*OH + CH_4	−3.430	—	1.79	0.30	—	−1.10
*CH_3	−1.740	1.94	—	0.20	−0.38	—
*OH	−3.279	—	1.79	0.31	—	−1.12
*CH_4	−0.494	2.35	—	0.15	−0.20	—
*OH_2	−0.963	—	2.06	0.21	—	−1.16

values of 2.26 V and 1.01 V on pristine MoS_2 and Cu (111) surfaces.[64] The overpotential for paths 1 to 3 is 1.21 V, and for path 5 is 1.33 V. Path 4 has the highest overpotential of 2.51 V, whilst also having the most negative limiting potential of −2.49 V. Therefore, path 6 is found to be the more probable pathway for Cu–MoS_2 due to its lower overpotential. From the free energy diagram (Fig. 5), it is obvious that hydrogenation of *OCHOH to form the *OCH_2OH intermediate (*via* path 6) has a comparatively smaller ΔG than that for forming the *CHO intermediate (*via* path 5) on the catalyst surface. Further, the subsequent hydrogenation of *OCH_2OH to form *OCH_2 is exothermic, and the *OCH_2 species also shows a strong adsorption on the SAC surface (E_{ads} = −0.858 eV, *cf.* Table 1). Therefore, it will be further reduced to *CH_2OH (if *H attacks the O atom) or *OCH_3 (if *H attacks the C atom) and yield another important C1 product, *$OHCH_3$, which is again an exothermic process overall. In contrast, path 2 shown in Fig. 5 is endothermic for the reduction step of *OCH_2 to *CH_2OH and then proceeds to the formation of *$OHCH_3$. So, it is worth noting that the formation of *OCH_3 from *OCH_2 is an another crucial step that is thermodynamically favorable. To summarize, Cu–MoS_2 has better catalytic performance for reducing CO_2 to CH_3OH with a lower overpotential than the pristine MoS_2, and the optimized reaction pathway (involving 6e$^-$ transfer) is path 6: CO_2 → *OCHO → *OCHOH → *OCH_2OH → *OCH_2 → *OCH_3 → *$OHCH_3$.

3.2.3 Eight-electron pathway: CH_4 formation. In this section, we discuss the CO_2RR process involving 8e$^-$ transfer for the formation of the ultimate C1 product CH_4 (methane). Same as for the formation of methanol, the reduction of CO_2 to CH_4 on Cu–MoS_2 SAC also follows six different paths, and in principle it undergoes two more hydrogenation steps. The free energy profile diagrams for the different pathways are illustrated in Fig. 6.

It can be seen from all the paths in Fig. 6 that doping with Cu leads to better catalytic performance than that of the pristine MoS_2 monolayer. As we know, the overall catalytic behavior relies on the individual pathways; the presence of a large barrier in the case of the pristine monolayer hinders the further reduction process. As observed in the 6e$^-$ transfer, the PDS is determined here by the stable intermediates *CO (path 1 to 4) and *OCHOH (path 5 and 6). The corresponding hydrogenation step yields a few feasible metastable intermediates: *CHO (path 1, 2, and 4), *COH (path 3), and *OCH_2OH (path 5 and 6) with the limiting potentials of −1.19, −2.49, and −0.84 V, respectively. It is worth pointing out here that in path 3, the protonation of *COH (where *H attacks the O atom) forms the highly unstable *C *via* dehydration, and it is considered to be the largest positive free energy change (overall) among the different paths, whilst also being highly endothermic. Similarly, the *H attack on the O atom of the *CHO intermediate to form *CHOH in path 1 also proceeds endothermically. In the case of the other paths (2, 4, 5 and 6, in which *H attacks the C atom), the catalytic conversion steps of *CHO → *OCH_2 (protonation) and *OCH_2OH → *OCH_2 (protonation followed

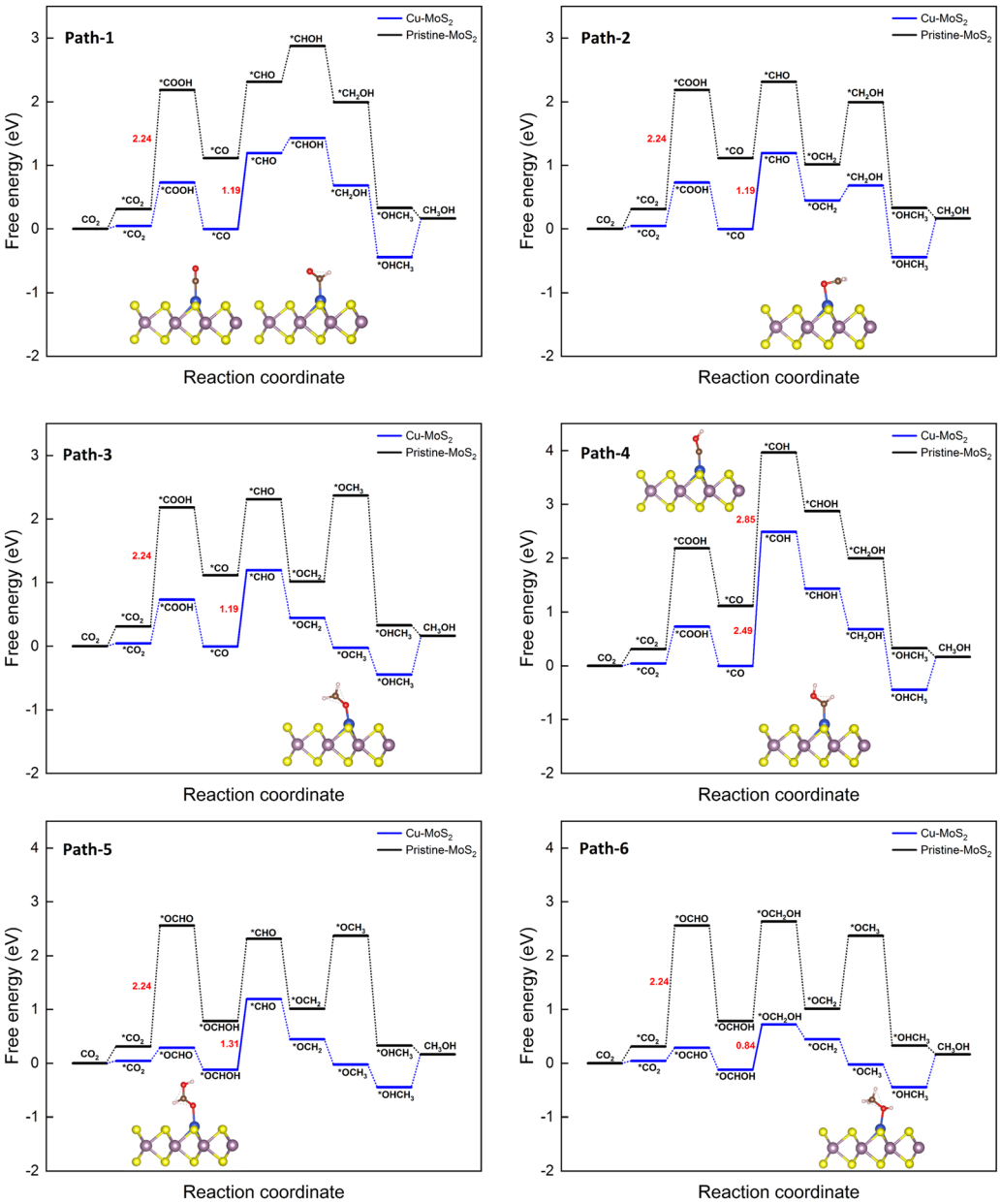

Fig. 5 Gibbs free energy diagrams for six different pathways of the CO_2RR towards CH_3OH on the MoS_2 monolayer with embedded Cu at 0 V *vs.* the RHE.

Table 2 The overpotentials (η) and limiting potentials (U_L) for the potential-determining steps (PDSs) of different pathways for the CO_2RR to CH_3OH on the MoS_2 monolayer with embedded Cu

CO_2RR	PDS	U_L (V)	η (V)
Path 1	*CO → *CHO	−1.19	1.21
Path 2	*CO → *CHO	−1.19	1.21
Path 3	*CO → *CHO	−1.19	1.21
Path 4	*CO → *COH	−2.49	2.51
Path 5	*OCHOH → *CHO	−1.31	1.33
Path 6	*OCHOH → *OCH_2OH	−0.84	0.86

by the dehydration) are exothermic processes. As the electrochemical reduction proceeds, the *OCH_3 intermediate can be easily formed, as seen in path 4, 5 and 6. The reduction reaction of *OCH_3 to *O + CH_4 (paths 4 and 6) is endothermic with a large ΔG (1.71 eV) and later it becomes the PDS for these paths, whereas the conversion of *OCH_3 to *$HOCH_3$ in path 5 is clearly exothermic. Therefore, path 5 is preferred, finally desorbing the CH_4 molecule successfully from the Cu–MoS_2 SAC surface. It can be concluded that path 5 could be a preferable (optimized) reduction pathway for CO_2 to CH_4 on Cu–MoS_2, proceeding *via* *OCH_2 → *OCH_3 → *$OHCH_3$ → *OH + CH_4 → H_2O.

Further, the calculated overpotentials and limiting potentials for the potential-determining steps of the different pathways for the CO_2RR to CH_4 on MoS_2 with embedded Cu are summarized in Table 3.

The lowest overpotential (η = 1.01 V) is obtained for the PDS of path 5, whereas the highest η (2.66 V) is obtained for path 3,

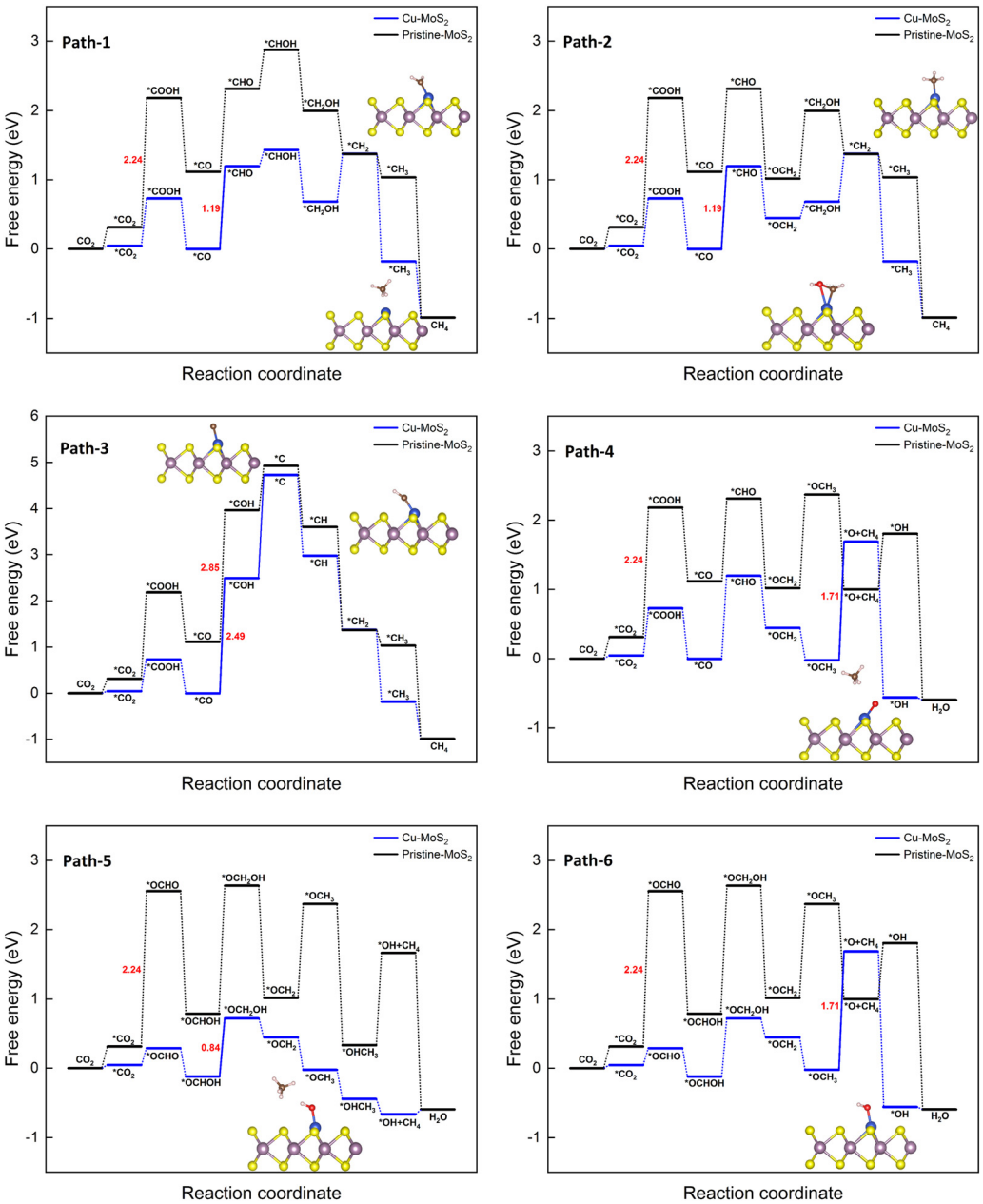

Fig. 6 Gibbs free energy diagrams for six different pathways of the CO_2RR towards CH_4 on the MoS_2 monolayer with embedded Cu at 0 V *vs.* the RHE.

with moderate values of η (1.36 and 1.88 V) for the rest of the paths. Note that the PDS for the preferred path 5 is the third hydrogenation step, but that for the other competing paths (4 and 6) is found to be the sixth hydrogenation step with a limiting potential (1.71 V) that is more than two-fold that of the preferred path 5. To assess the efficiency of Cu-doped MoS_2, the overpotential of the pristine MoS_2 monolayer is also estimated for the PDS of $*CO_2 \rightarrow *COOH$); here η = 2.41 V, which is almost three-times higher than that of the preferred path on Cu–MoS_2. So, it is verified that the MoS_2 SAC with embedded Cu shows an excellent catalytic activity for the reduction of CO_2 to CH_4 (*via* optimized path 5) compared to the pristine MoS_2. In order to highlight our result, we have shown a comparison of our limiting potential with that of other reported CO_2RR catalysts, such as Fe–C_3N_4,[61] Zr@C_2N,[65] Cu (111) and Cu–phosphorene,[64] in Fig. 7.

Table 3 The overpotentials (η) and limiting potentials (U_L) for the potential-determining steps (PDSs) of different pathways for the CO_2RR to CH_4 on the MoS_2 monolayer with embedded Cu

CO_2RR	PDS	U_L (V)	η (V)
Path 1	$*CO \rightarrow *CHO$	−1.19	1.36
Path 2	$*CO \rightarrow *CHO$	−1.19	1.36
Path 3	$*CO \rightarrow *COH$	−2.49	2.66
Path 4	$*OCH_3 \rightarrow *O + CH_4$	−1.71	1.88
Path 5	$*OCHOH \rightarrow *OCH_2OH$	−0.84	1.01
Path 6	$*OCH_3 \rightarrow *O + CH_4$	−1.71	1.88

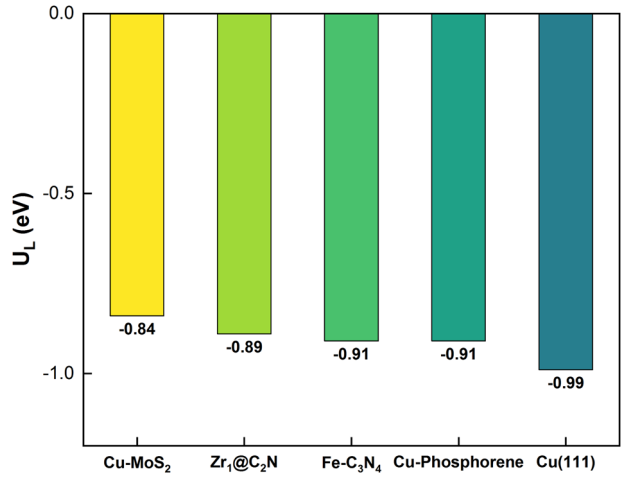

Fig. 7 The comparison of the limiting potential from our model (Cu-doped MoS_2 SAC) with that of other reported catalysts for the reduction of CO_2 to CH_4.

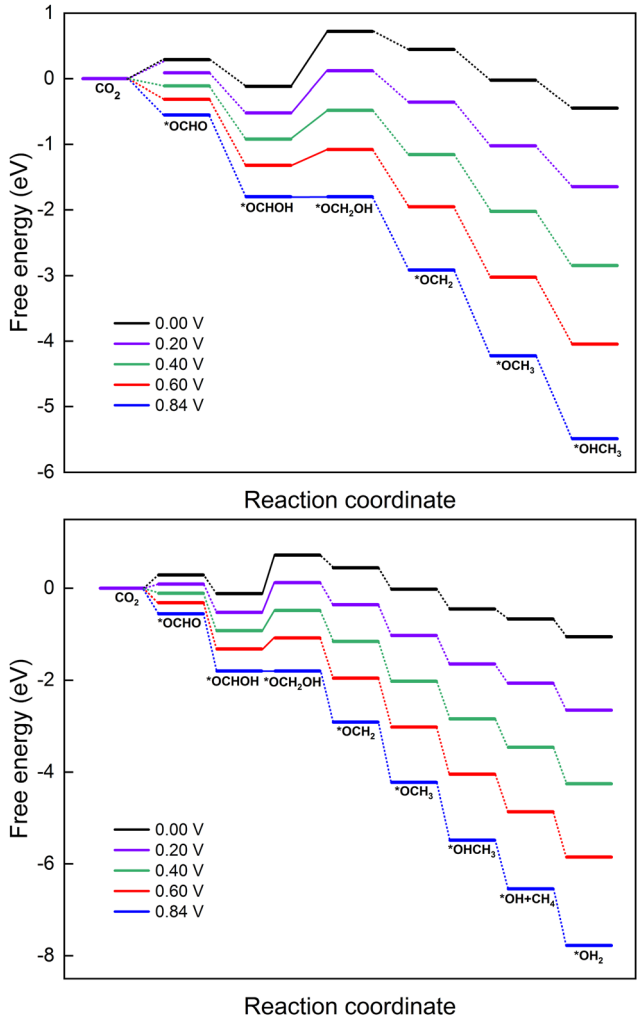

Fig. 8 Impact of applied potential on the free energy profile of the CO_2RR to CH_3OH (top panel) and CH_4 (bottom panel) on the Cu–MoS_2 monolayer. The legends for the different applied potentials are included in the respective panels.

3.3 Impact of applied potential on the CO_2RR on MoS_2 with embedded Cu

In this section, the reaction mechanism for the electrocatalytic reduction of CO_2 to methanol or methane on MoS_2 with embedded Cu is explored under different applied potentials (U). The optimized reduction pathways for producing CH_3OH (path 6 from Fig. 5) and CH_4 (path 5 from Fig. 6) have been selected based on the aforementioned discussion. The effect of applied potential on these optimized paths (6 and 5) is presented in the free energy diagrams shown in Fig. 8. Both the six- and eight-electron reaction pathways for the formation of products CH_3OH and CH_4 are sensitive to the applied potential, which neutralizes the barrier of the PDS and makes all the elementary reactions exothermic processes. The ΔG_{max} for producing CH_3OH and CH_4 decreases when increasing the applied potential from 0 to 0.84 V, which indeed speeds up the CO_2RR process. As mentioned, the PDS of the CO_2RR on Cu–MoS_2 is the formation of $*OCH_2OH$ and the uphill energy step becomes exothermic at the applied potential of 0.84 V. The required external applied potential (U) can be determined from the lowest limiting potential (U_L) value of the PDS for the specific reduction pathway. Since the PDS for formation of both products CH_3OH and CH_4 exhibits a U_L of $\sim$0.84 V, we required the same magnitude of U to trigger the CO_2RR on the Cu–MoS_2 SAC.

4 Conclusions

In this work, we have studied the catalytic activity of the electrochemical reduction of CO_2 to C1 products on a Cu–MoS_2 monolayer single-atom catalyst by performing DFT calculations. The computational results reveal that Cu embedded in a sulfur vacancy in the MoS_2 monolayer effectively increases the catalytic activity of CO_2RR relative to that of the pristine MoS_2. The different pathways, involving several elementary reactions *via* coupled proton–electron transfers, were explored, namely $2e^-$, $6e^-$, and $8e^-$ pathways. The reaction mechanisms of all pathways and their PDSs are discussed in terms of free energy diagrams and adsorption energies. The strong electronic interactions between the Cu-3d orbital and those of the intermediates formed during the hydrogenation steps are confirmed by PDOS and charge density difference analysis. The main conclusions drawn from the present study are summarized as follows:

- The CO_2 shows a strong adsorption on the MoS_2 monolayer with embedded Cu, with $E_{ads} = -0.474$ eV.
- In view of the CO_2RR *vs.* HER, the Cu–MoS_2 SAC effectively suppresses the HER by setting a large energy barrier to the HER, and as a result, the adsorption of *H ($E_{ads} = 0.419$ eV) is unfavourable.
- Six different paths involving $6e^-$ and $8e^-$ transfer were explored for the CO_2RR, and it was noticed that the formation of both CH_3OH and CH_4 follows the same reduction pathway, with the lowest limiting potential of $\sim$0.84 V.
- During the hydrogenation process, which decides the PDS for the CO_2RR, the proton–electron pair ($H^+ + e^-$) mostly prefers

to attack the C atom rather than the O atom of the adsorbed CO_2 on the Cu–MoS_2 SAC.

• The PDSs of the optimized pathways for the electrocatalytic reduction of CO_2 to HCOOH and CH_4 are $CO_2 \rightarrow *OCHO$ and $*OCHOH \rightarrow *OCH_2OH$.

• Some notable intermediates, *CO, *C and $*OCH_2$, are formed *via* protonation followed by dehydration during the course of catalytic reduction of CO_2.

• The lowest overpotentials of 0.86 and 1.01 V were achieved for formation of methanol and methane, respectively, which play a significant role in the CO_2RR.

• As a result, the formation of methane (involving $8e^-$ transfer) is found to be most favored among the C1 products, *i.e.*, CO, HCOOH, CH_3OH, and CH_4, and the overall process is exothermic.

• From the free energy diagram, the most optimized pathway for the efficient catalytic reduction of CO_2 to CH_4 is path 5, which is given as: $CO_2 \rightarrow *OCHO \rightarrow *OCHOH \rightarrow *OCH_2OH \rightarrow *OCH_2 \rightarrow *OCH_3 \rightarrow *OHCH_3 \rightarrow *OH + CH_4 \rightarrow H_2O$.

With the above findings, we conclude that the MoS_2 monolayer with embedded Cu is a more promising electrocatalyst for an efficient CO_2RR process than the pristine MoS_2.

Conflicts of interest

There are no conflicts of interest to declare.

Acknowledgements

The first author (TD) thanks Pondicherry University for the research fellowship. The computational facilities provided by the UGC-SAP under the Department of Special Assistance (DSA-I), New Delhi, are gratefully acknowledged. The project was supported by the Researchers Supporting Project number (RSP2023R143), King Saud University, Riyadh, Saudi Arabia.

References

1 D. Lüthi, M. Le Floch, B. Bereiter, T. Blunier, J.-M. Barnola, U. Siegenthaler, D. Raynaud, J. Jouzel, H. Fischer and K. Kawamura, *et al.*, *Nature*, 2008, **453**, 379–382.
2 S. J. Davis, K. Caldeira and H. D. Matthews, *Science*, 2010, **329**, 1330–1333.
3 H. Class, A. Ebigbo, R. Helmig, H. K. Dahle, J. M. Nordbotten, M. A. Celia, P. Audigane, M. Darcis, J. Ennis-King and Y. Fan, *et al.*, *Comput. Geosci.*, 2009, **13**, 409–434.
4 L. Giordano, D. Roizard and E. Favre, *Int. J. Greenhouse Gas Control*, 2018, **68**, 146–163.
5 S. Liu, H. Ling, J. Lv, H. Gao, Y. Na and Z. Liang, *Ind. Eng. Chem. Res.*, 2019, **58**, 20461–20471.
6 B. O. Demars, G. M. Gslason, J. S. Ólafsson, J. R. Manson, N. Friberg, J. M. Hood, J. J. Thompson and T. E. Freitag, *Nat. Geosci.*, 2016, **9**, 758–761.
7 J. Shi, Y. Jiang, Z. Jiang, X. Wang, X. Wang, S. Zhang, P. Han and C. Yang, *Chem. Soc. Rev.*, 2015, **44**, 5981–6000.
8 P. Usubharatana, D. McMartin, A. Veawab and P. Tontiwachwuthikul, *Ind. Eng. Chem. Res.*, 2006, **45**, 2558–2568.
9 W. Zhang, Y. Hu, L. Ma, G. Zhu, Y. Wang, X. Xue, R. Chen, S. Yang and Z. Jin, *Adv. Sci.*, 2018, **5**, 1700275.
10 Y. Chen, C. W. Li and M. W. Kanan, *J. Am. Chem. Soc.*, 2012, **134**, 19969–19972.
11 D. Sun, X. Xu, Y. Qin, S. P. Jiang and Z. Shao, *ChemSusChem*, 2020, **13**, 39–58.
12 W. J. Durand, A. A. Peterson, F. Studt, F. Abild-Pedersen and J. K. Nørskov, *Surf. Sci.*, 2011, **605**, 1354–1359.
13 S. Liu, H. Yang, X. Su, J. Ding, Q. Mao, Y. Huang, T. Zhang and B. Liu, *J. Energy Chem.*, 2019, **36**, 95–105.
14 S. Nitopi, E. Bertheussen, S. B. Scott, X. Liu, A. K. Engstfeld, S. Horch, B. Seger, I. E. Stephens, K. Chan and C. Hahn, *et al.*, *Chem. Rev.*, 2019, **119**, 7610–7672.
15 X.-F. Yang, A. Wang, B. Qiao, J. Li, J. Liu and T. Zhang, *Acc. Chem. Res.*, 2013, **46**, 1740–1748.
16 R. Qin, K. Liu, Q. Wu and N. Zheng, *Chem. Rev.*, 2020, **120**, 11810–11899.
17 L. Zhang, K. Doyle-Davis and X. Sun, *Energy Environ. Sci.*, 2019, **12**, 492–517.
18 B. Qiao, A. Wang, X. Yang, L. F. Allard, Z. Jiang, Y. Cui, J. Liu, J. Li and T. Zhang, *Nat. Chem.*, 2011, **3**, 634–641.
19 J. H. Liu, L.-M. Yang and E. Ganz, *ACS Sustainable Chem. Eng.*, 2018, **6**, 15494–15502.
20 H. Yang, Q. Lin, C. Zhang, X. Yu, Z. Cheng, G. Li, Q. Hu, X. Ren, Q. Zhang and J. Liu, *et al.*, *Nat. Commun.*, 2020, **11**, 1.
21 N. Han, Y. Wang, L. Ma, J. Wen, J. Li, H. Zheng, K. Nie, X. Wang, F. Zhao and Y. Li, *et al.*, *Chem*, 2017, **3**, 652–664.
22 Z. Wang, J. Zhao and Q. Cai, *Phys. Chem. Chem. Phys.*, 2017, **19**, 23113–23121.
23 M. Donarelli, S. Prezioso, F. Perrozzi, F. Bisti, M. Nardone, L. Giancaterini, C. Cantalini and L. Ottaviano, *Sens. Actuators, B*, 2015, **207**, 602–613.
24 D. B. Putungan, S.-H. Lin, C.-M. Wei and J.-L. Kuo, *Phys. Chem. Chem. Phys.*, 2015, **17**, 11367–11374.
25 H. Hwang, H. Kim and J. Cho, *Nano Lett.*, 2011, **11**, 4826–4830.
26 B. Radisavljevic, A. Radenovic, J. Brivio, V. Giacometti and A. Kis, *Nat. Nanotechnol.*, 2011, **6**, 147–150.
27 O. Lopez-Sanchez, D. Lembke, M. Kayci, A. Radenovic and A. Kis, *Nat. Nanotechnol.*, 2013, **8**, 497–501.
28 K. F. Mak, C. Lee, J. Hone, J. Shan and T. F. Heinz, *Phys. Rev. Lett.*, 2010, **105**, 136805.
29 A. Splendiani, L. Sun, Y. Zhang, T. Li, J. Kim, C.-Y. Chim, G. Galli and F. Wang, *Nano Lett.*, 2010, **10**, 1271–1275.
30 S. Zhao, J. Xue and W. Kang, *Chem. Phys. Lett.*, 2014, **595–596**, 35–42.
31 L. S. Byskov, J. K. Nørskov, B. S. Clausen and H. Topsøe, *Catal. Lett.*, 2000, **64**, 95–99.
32 D. Voiry, R. Fullon, J. Yang, C. de Carvalho Castro e Silva, R. Kappera, I. Bozkurt, D. Kaplan, M. J. Lagos, P. E. Batson and G. Gupta, *et al.*, *Nat. Mater.*, 2016, **15**, 1003–1009.

33 H. Luo, Y. Cao, J. Zhou, J. Feng, J. Cao and H. Guo, *Chem. Phys. Lett.*, 2016, **643**, 27–33.
34 D. Chen, X. Zhang, J. Tang, H. Cui and Y. Li, *Appl. Phys. A: Mater. Sci. Process.*, 2018, **124**, 194.
35 Y. H. Zhang, J. L. Chen, L. J. Yue, H. L. Zhang and F. Li, *Comput. Theor. Chem.*, 2017, **1104**, 12–17.
36 D. Ma, W. Ju, T. Li, X. Zhang, C. He, B. Ma, Z. Lu and Z. Yang, *Appl. Surf. Sci.*, 2016, **383**, 98–105.
37 J. Zhao, J. Zhao and Q. Cai, *Phys. Chem. Chem. Phys.*, 2018, **20**, 9248–9255.
38 D. Ma, Y. Tang, G. Yang, J. Zeng, C. He and Z. Lu, *Appl. Surf. Sci.*, 2015, **328**, 71–77.
39 T. Jitwatanasirikul, T. Roongcharoen, C. Chitpakdee, S. Jungsuttiwong, P. Poldorn, K. Takahashi and S. Namuangruk, *New J. Chem.*, 2021, **45**, 17407–17417.
40 H. P. Komsa and A. V. Krasheninnikov, *Phys. Rev. B: Condens. Matter Mater. Phys.*, 2015, **91**, 125304.
41 H. Nan, Z. Wang, W. Wang, Z. Liang, Y. Lu, Q. Chen, D. He, P. Tan, F. Miao and X. Wang, *et al.*, *ACS Nano*, 2014, **8**, 5738–5745.
42 G. Liu, A. W. Robertson, M. M.-J. Li, W. C. Kuo, M. T. Darby, M. H. Muhieddine, Y.-C. Lin, K. Suenaga, M. Stamatakis and J. H. Warner, *et al.*, *Nat. Chem.*, 2017, **9**, 810–816.
43 Y. Hori, A. Murata and R. Takahashi, *J. Chem. Soc., Faraday Trans. 1*, 1989, **85**, 2309–2326.
44 Y. Hori, H. Wakebe, T. Tsukamoto and O. Koga, *Electrochim. Acta*, 1994, **39**, 1833–1839.
45 D. Joseph, M. Navaneethan, R. Abinaya, S. Harish, J. Archana, S. Ponnusamy, K. Hara and Y. Hayakawa, *Appl. Surf. Sci.*, 2020, **505**, 144066.
46 W. Kohn and L. J. Sham, *Phys. Rev.*, 1965, **140**, A1133–A1138.
47 G. Kresse and D. Joubert, *Phys. Rev. B: Condens. Matter Mater. Phys.*, 1999, **59**, 1758–1775.
48 P. E. Blöchl, *Phys. Rev. B: Condens. Matter Mater. Phys.*, 1994, **50**, 17953–17979.
49 G. Kresse and J. Furthmüller, *Phys. Rev. B: Condens. Matter Mater. Phys.*, 1996, **54**, 11169–11186.
50 J. P. Perdew, K. Burke and M. Ernzerhof, *Phys. Rev. Lett.*, 1996, **77**, 3865–3868.
51 S. Grimme, J. Antony, S. Ehrlich and H. Krieg, *J. Chem. Phys.*, 2010, **132**, 154104.
52 H. J. Monkhorst and J. D. Pack, *Phys. Rev. B: Solid State*, 1976, **13**, 5188–5192.
53 G. Henkelman, A. Arnaldsson and H. Jónsson, *Comput. Mater. Sci.*, 2006, **36**, 354–360.
54 E. Sanville, S. D. Kenny, R. Smith and G. Henkelman, *J. Comput. Chem.*, 2007, **28**, 899–908.
55 J. K. Nørskov, J. Rossmeisl, A. Logadottir, L. Lindqvist, J. R. Kitchin, T. Bligaard and H. Jonsson, *J. Phys. Chem. B*, 2004, **108**, 17886–17892.
56 B. Zhao, C. Li, L. Liu, B. Zhou, Q. Zhang, Z. Chen and Z. Tang, *Appl. Surf. Sci.*, 2016, **382**, 280–287.
57 B. Xiao, P. Zhang, L. Han and Z. Wen, *Appl. Surf. Sci.*, 2015, **354**, 221–228.
58 W. Cong, Z. Tang, X. Zhao and J. Chu, *Sci. Rep.*, 2015, **5**, 9361.
59 A. A. Peterson, F. Abild-Pedersen, F. Studt, J. Rossmeisl and J. K. Nørskov, *Energy Environ. Sci.*, 2010, **3**, 1311–1315.
60 Y. Li, S. H. Chan and Q. Sun, *Nanoscale*, 2015, **7**, 8663–8683.
61 C. Guo, T. Zhang, X. Deng, X. Liang, W. Guo, X. Lu and C.-M. L. Wu, *ChemSusChem*, 2019, **12**, 5126–5132.
62 G. Ren, J. Sun, S. Zhai, L. Yang, T. Yu, L. Sun and W. Deng, *Cell Rep. Phys. Sci.*, 2022, **3**, 100705.
63 S. Zhao, S. Li, T. Guo, S. Zhang, J. Wang, Y. Wu and Y. Chen, *Nano-Micro Lett.*, 2019, **11**, 1–19.
64 H. P. Zhang, R. Zhang, C. Sun, Y. Jiao and Y. Zhang, *Nanoscale*, 2021, **13**, 20541–20549.
65 A. Hassan, I. Anis, S. Shafi, A. Assad, A. Rasool, R. Khanam, G. A. Bhat, S. Krishnamurty and M. A. Dar, *ACS Appl. Nano Mater.*, 2022, **5**, 15409–15417.

